Supporting Information

Molecularly Engineered Potential of d-Orbital Modulated Iron-Bridged Delaminated MBene for Rechargeable Zn–Air Batteries

Seung Woong Nam,[a] Thanh Hai Nguyen,[a] Duy Thanh Tran,[a] Van An Dinh,[b] Thi Thuy Nga Ta,[c] Chung-Li Dong,[c] Nam Hoon Kim,[a] Joong Hee Lee[a,d*]

[a] Dept. of Nano Convergence Engineering, Jeonbuk National University, Jeonju, Jeonbuk 54896, Republic of Korea.

[b] Department of Precision Engineering, Graduate School of Engineering, Osaka University, 2-1, Yamada-oka, Suita, Osaka 565-0871, Japan.

[c] Department of Physics, Tamkang University, New Taipei City, Taiwan.

[d] Carbon Composite Research Centre, Department of Polymer & Nanoscience and Technology, Jeonbuk National University, Jeonju, Jeonbuk 54896, Republic of Korea.

Materials and Methods

Chemicals

The MoAlB MAB (400 mesh) and Mo_2Ga_2C MAX (400 mesh) powders were purchased from the Laizhou Kai Kai Ceramic Materials Co., Ltd. (China). L-Ascorbic acid ($C_6H_8O_6$, 99%), iron(II) phthalocyanine ($C_{32}H_{16}FeN_8$, dye content ~ 90%), platinum on graphitized carbon (Pt/C, 20 wt% loading), tetramethylammonium hydroxide (TMAOH) [$(CH_3)_4N(OH)$, 25wt% in H_2O], hydrofluoric acid (HF, 48 %) and ruthenium(IV) oxide (RuO_2, 99.9 %) were provided by Sigma-Aldrich Co. (Korea). Potassium hydroxide (KOH, 85%), sodium hydroxide (NaOH, 98%), dimethylformamide (DMF) and isopropyl alcohol (C_3H_7OH, 99.9%) were obtained from Samchun Chemical Co. (Korea). platinum on graphitized carbon (Pt/C, 20 wt% loading), All chemicals and reagents are directly used as-received products without further purification.

Material characterization

The scanning electron microscopy (SEM) imaging was probed on a Supra 40 VP microscope (Zeiss Co., Germany). The high-resolution transmission electron microscopy (HR−TEM) and high-angle annular dark-field (HAADF)–STEM imaging was performed on a JEM−ARM200F microscope (JEOL, Japan) equipped with energy-dispersive X-ray spectroscopy (EDS). The Fe K-edge X-ray absorption spectroscopy (XAS), including XANES, EXAFS, and WT-EXAFS were conducted at BL17C – TLS, National Synchrotron Radiation Research Center (Taiwan). The X-ray photoelectron spectroscopy (XPS) was conducted using a Nexsa XPS system (Thermo Fisher Scientific Inc., USA) equipped with X-ray source (Al Kα). Raman spectra was recorded using a Laser Raman Microscopy with a laser wavelength of 532 nm (Nanophoton, Japan). X-ray diffraction (XRD) was performed to reveal the crystallinity of samples on a D/Max 2500 V/PC system (Japan) with 2θ ranging from 5 to 80°. An ASAP 2020 Plus system (Micromeritics Instrument Co., USA) was utilized to measure the specific surface area through N_2 adsorption-desorption isotherms.

Electrochemical analyses

All electrochemical performance was performed on a CHI Instruments (CHI660D) integrated with a conventional three-electrode cell. A rotating disk electrode (RDE) and rotating ring disk electrode (RRDE) with a glassy carbon (5 mm in diameter) and a Pt ring electrode was served as working electrode. The ORR catalyst ink was prepared by dispersing 5.0 mg of active material and 5.0 mg of carbon black in 1.0 mL of IPA with 50 μL of 5wt.% Nafion and sonicated for 1 h in iced bath. Then, an appropriate amount of the ink was drop-cast on RDE (or RRDE) as working electrode and dried naturally. The catalyst loading was fixed at 0.56 mg cm^{-2}. The working electrode was also polished carefully with alumina suspension on micro-cloth polishing pad. The reference and counter electrodes are Ag/AgCl (sat. KCl) and graphite

rod, respectively. All potentials were converted to reversible reference electrode (RHE) by using Nerst equation.

$$E_{RHE} = E_{measured} + E_{Ag/AgCl}^0 + 0.0592 \times pH_) \quad (1)$$

The solution electrolyte was purged with high-purity O_2 (or N_2) gas for at least 30 min before cyclic voltammetry (CV) measurements. Linear sweep voltammetry (LSV) was employed to determine the catalytic activity of samples in O_2-saturated electrolyte from 1.2 to 0.2 V (vs. RHE) at a scan rate of 5.0 mV s^{-1} and a rotating speed of 1600 rpm. The Koutecky-Levich equation was used to calculate the electron transfer number (n) according to the LSV obtained at different rotation rates:

$$\frac{1}{j} = \frac{1}{j_k} + \frac{1}{j_L} = \frac{1}{j_k} + \frac{1}{B\sqrt{\omega}} \quad (2)$$

$$B = 0.62 \times D_{O_2}^{3/2} \times C_{O_2} \times v^{-1/6} \times n \times F \quad (3)$$

Where j, j_k and j_L are measured, kinetic, and limiting current densities, respectively. ω is the angular velocity. D_{O2} is diffusivity coefficient of oxygen (1.9×10^{-5} cm^2 s^{-1}). C_{O2} is bulk concentration of oxygen (1.2×10^{-6} mol cm^{-3}). v (0.01 cm^2 s^{-1}) is the kinematic viscosity of electrolyte. n is the electron transfer number. F is Faraday constant (96 485 C mol^{-1}).

The hydrogen peroxide yield (H_2O_2 %) and obvious electron transfer number during ORR were carried out using RRDE technique. In this study, we fixed the ring potential at 1.3 V (vs. RHE).

$$H_2O_2\% = 200 \times \frac{\dfrac{I_r}{N}}{I_d + \dfrac{I_r}{N}} \quad (4)$$

$$n = 4 \times \frac{I_d}{I_d + \dfrac{I_r}{N}}$$

(5)

Where I_r and I_d are ring and disk current, respectively. N is the H_2O_2 collection coefficient (N=0.4).

For the OER test, typically, the catalyst ink was prepared by dispersing 2.5 mg of active material and 0.5 mg of carbon black in 700 μL of IPA with 50 μL of 5wt.% Nafion and sonicated for 1.0 h in iced bath. The ink was further drop-cast on carbon paper (1.0 cm^2, 2.5 mg cm^{-2}), followed by the vacuum-drying for overnight. LSV was used to evaluate the catalytic activity of samples in 1.0 M KOH electrolyte solution at a scan rate of 5.0 mV s^{-1}. Electrochemical impedance spectroscopy (EIS) was conducted with an amplitude of 5.0 mV in frequency range 10^5 to 10^{-1} Hz at open circuit voltage. The double-layer capacitance (C_{dl}) was assessed through CV curves at the non-Faradaic region with different scan rate (10 – 100 mV s^{-1}). The long-term stability of the as-prepared samples was measured by chronoamperometric (i-t) technique in static condition.

ZAB performance test

The aqueous rechargeable ZAB cell was designed with the use of 6.0 M KOH containing 0.2 M Zn(OAc)$_2$ as electrolyte, the developed catalyst-loaded CC (1×1 cm^2) as air cathode, and Zn foil (0.25 mm in thickness) as anode. The galvanostatic charge-discharge cycling durability was tested on Multichannel P'stat/G'stat WMPG1000S (WonATech, Korea) with 30 min of discharging and 30 min of charging at a current density of 10 mA cm^{-2}. The fabrication of prototype solid-state ZAB with the use of a gel electrolyte follows our previous publications.[3] The capacity ratio anode (negative)-to-cathode (positive) (N/P) of cell was calculated as follows:
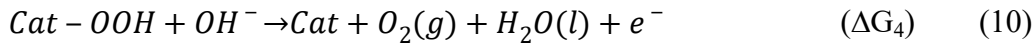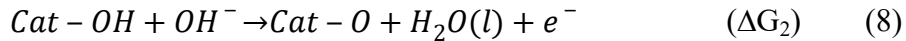
$$N/P \ ratio = \frac{Capacity \ of \ Zinc \ anode}{Capacity \ of \ air \ cathode} \qquad (6)$$

Where the capacity of Zn anode was taken from theoretical capacity of Zinc (820 mAh/g).

Computational methods

All density functional theory (DFT) calculations were performed using Vienna ab initio simulation package (VASP).[4,5] We used generalized gradient approximation and Perdew-Burke-Ernzerhof (GGA-PBE) functional together with default projector augmented wave (PAW) pseudopotentials.[6] Spin polarization and D3 empirical correction were considered during geometry optimizations.[7] A 500 eV was used for kinetic energy cutoff and the geometry structures were fully relaxed until the residual forces were less than 0.02 eV Å^{-1}. A 15 Å vacuum layer was added in z-axis to avoid self-interaction between periodic slabs. Due to the large size of super-cell model, Γ-center k-point (1×1×1) was used for our calculations. VASPKIT and VESTA were used for data processing and visualization.[8]

In this study, we adapted the four-electron reaction pathway for OER and ORR in alkaline media as follows.[9,10]

$$Cat + OH^- \rightarrow Cat - OH + e^- \qquad (\Delta G_1) \qquad (7)$$

$$Cat - OH + OH^- \rightarrow Cat - O + H_2O(l) + e^- \qquad (\Delta G_2) \qquad (8)$$

$$Cat - O + OH^- \rightarrow Cat - OOH + e^- \qquad (\Delta G_3) \qquad (9)$$

$$Cat - OOH + OH^- \rightarrow Cat + O_2(g) + H_2O(l) + e^- \qquad (\Delta G_4) \qquad (10)$$

where "Cat" stands for the active centers on the electrocatalyst. The ORR pathway is a reserve reaction to OER pathway.

The Gibbs free energy of each step is calculated as follows.

$$\Delta G = \Delta E + \Delta E_{ZPE} - T\Delta S \qquad (11)$$

where ΔE is the change in total energy computed by DFT. ΔE_{ZPE} and ΔS are the change in zero-

point energy and entropy, respectively. T is temperature (298.15 K).

The theoretical overpotential (η) of OER and ORR are defined as follows.

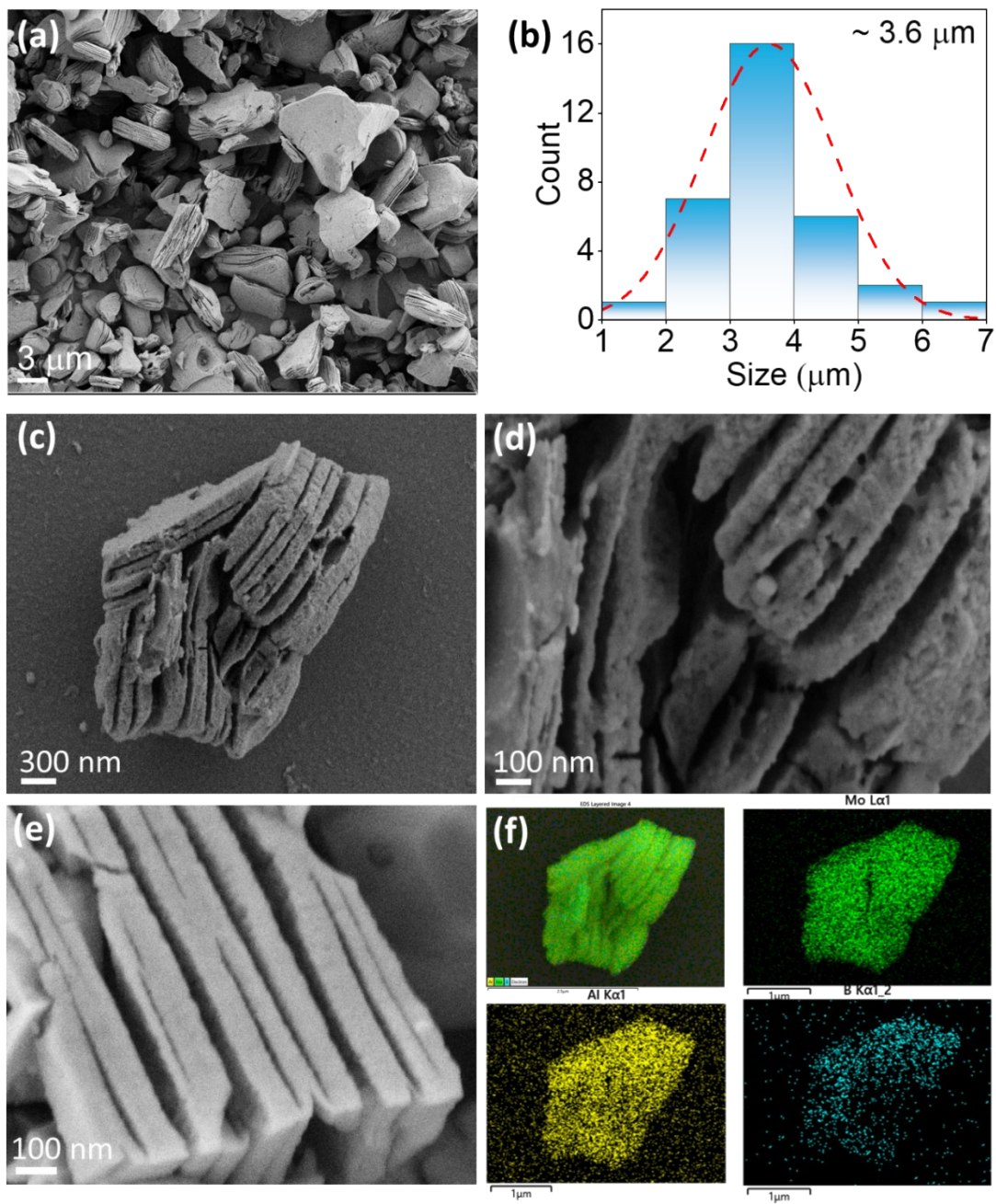$$\eta_{OER} = \frac{max\{\Delta G_1, \Delta G_2, \Delta G_3, \Delta G_4\}}{e} - 1.23 \; (V) \tag{12}$$

$$\eta_{ORR} = 1.23 - \frac{min\{\Delta G_1, \Delta G_2, \Delta G_3, \Delta G_4\}}{e} \; (V) \tag{13}$$
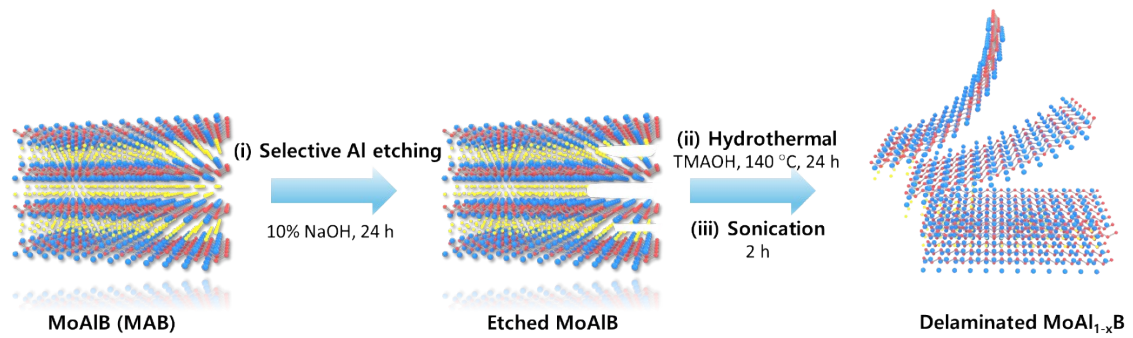
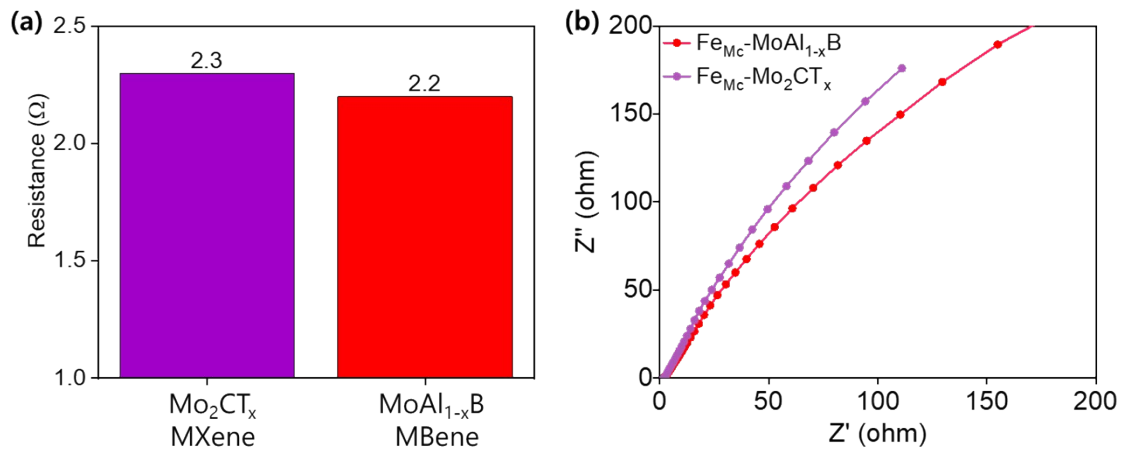**Figure S1**. The schematic illustration for the preparation of partially delaminated $MoAl_{1-x}B$ material.
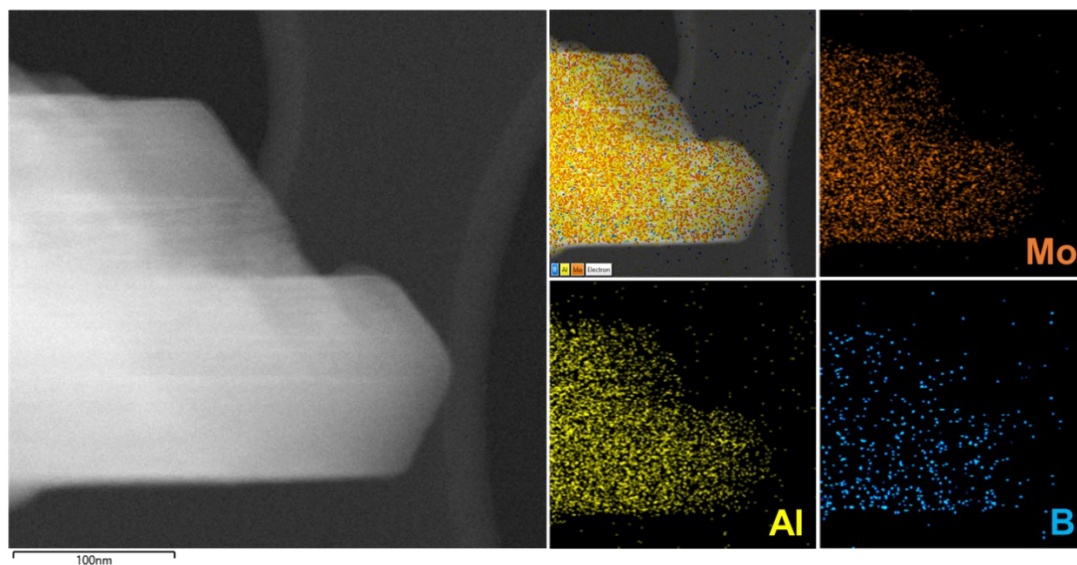
Figure S2. SEM-EDS mapping images of the bulk MAB material.

Figure S3. (a) Low-magnification SEM image and (b) size distribution of MoAl$_{1-x}$B material; (c-e) High-magnification SEM images and (f) EDS mapping images of a delaminated MoAl$_{1-x}$B particle.

Figure S4. Electrical conductivity of MBene and MXene measured by four-robe method; (b) Interfacial charge transfer resistance of Fe_{Mc}-MBene and Fe_{Mc}-MXene hybrids measured by EIS analysis.
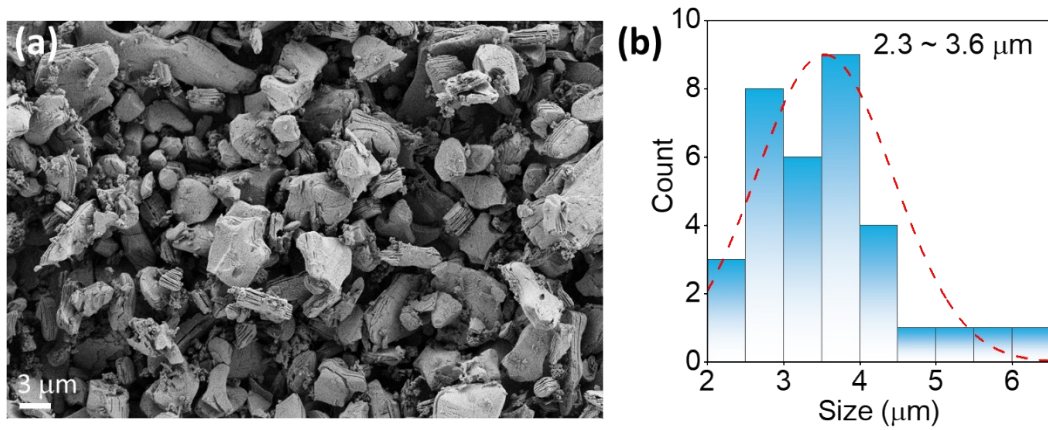
Figure S5. (a) Low-magnification SEM image of Fe_{Mc}–$MoAl_{1-x}B$ material and (b) its particle size distribution.
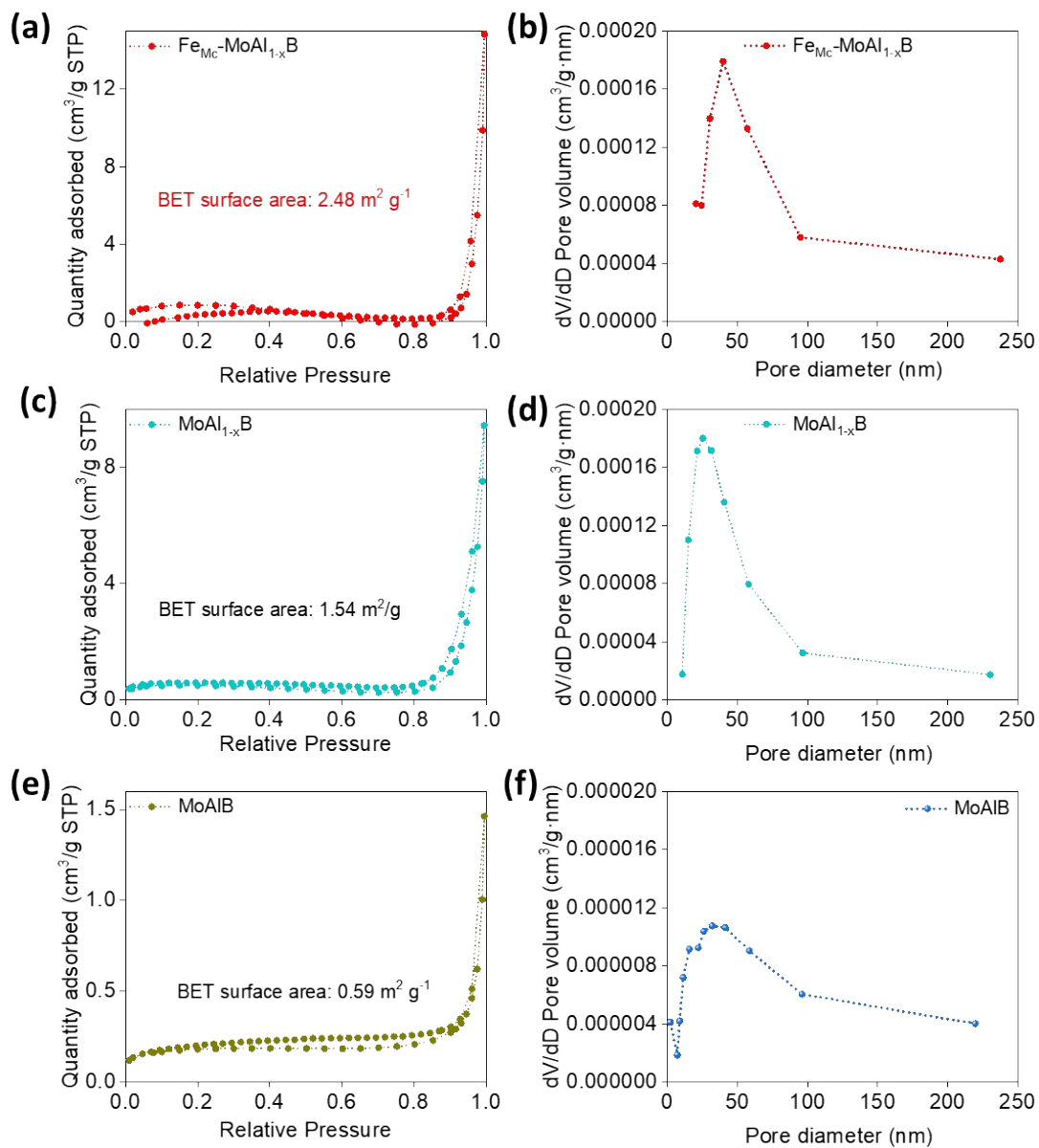
Figure S6. (a, c, e) Nitrogen adsorption-desorption isotherms and (b, d, f) pore distribution of bulk MAB, $MoAl_{1-x}B$, and $Fe_{Mc}–MoAl_{1-x}B$ material.
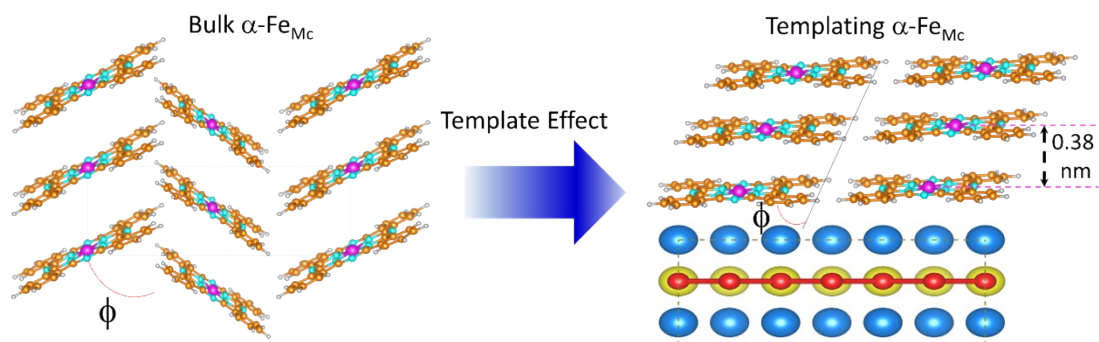
Figure S7. Schematics of the unit cells of bulk α-Fe$_{Mc}$ cluster and templating α-Fe$_{Mc}$ cluster on MoAl1xxB substrate.
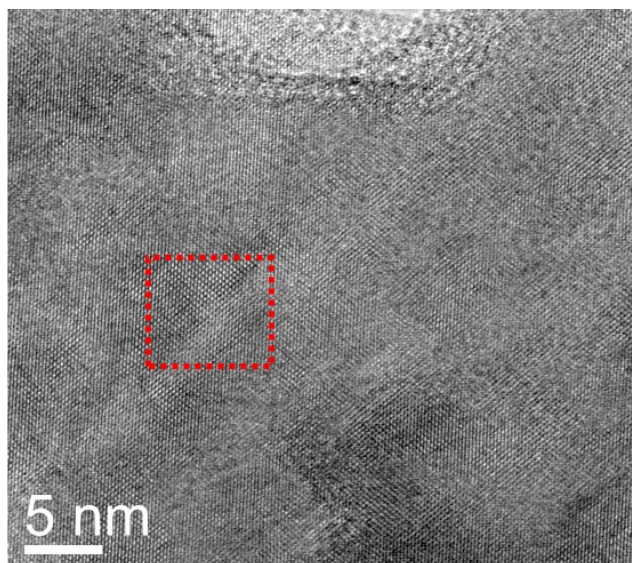
Figure S8. HR-TEM image from a small nano-size area of $Fe_{Mc}-MoAl_{1-x}B$ material.
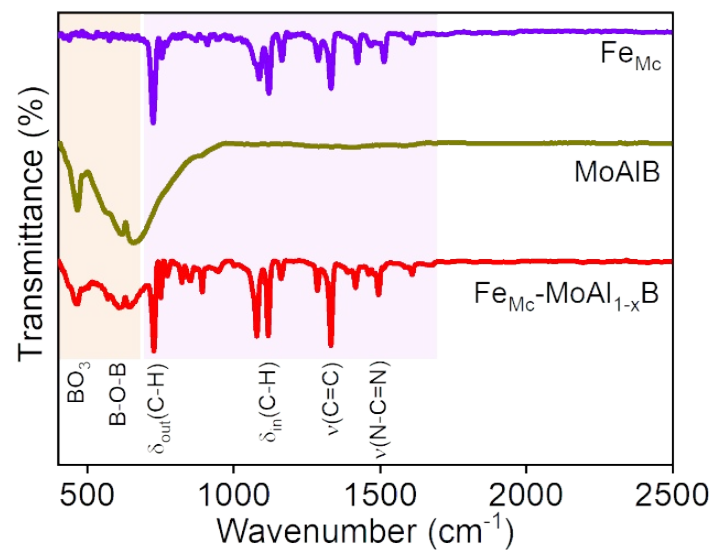
Figure S9. FT-IR spectra of MAB, Fe_{Mc}, and Fe_{Mc}–$MoAl_{1-x}B$ material.
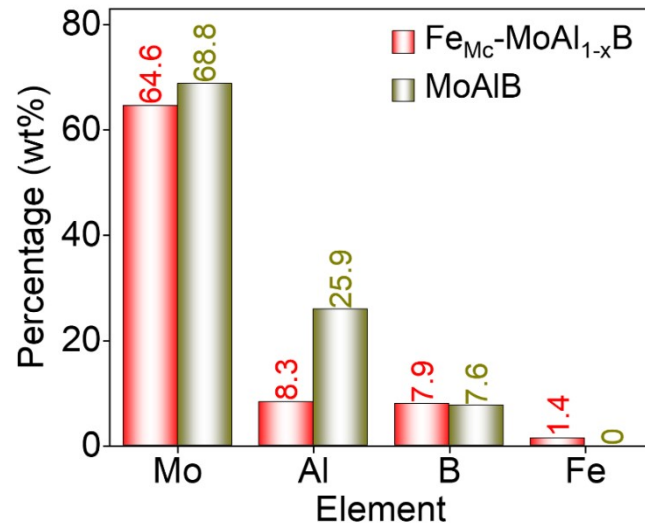
Figure S10. ICP-OES result of MoAlB and Fe_{Mc}–$MoAl_{1-x}B$ materials.
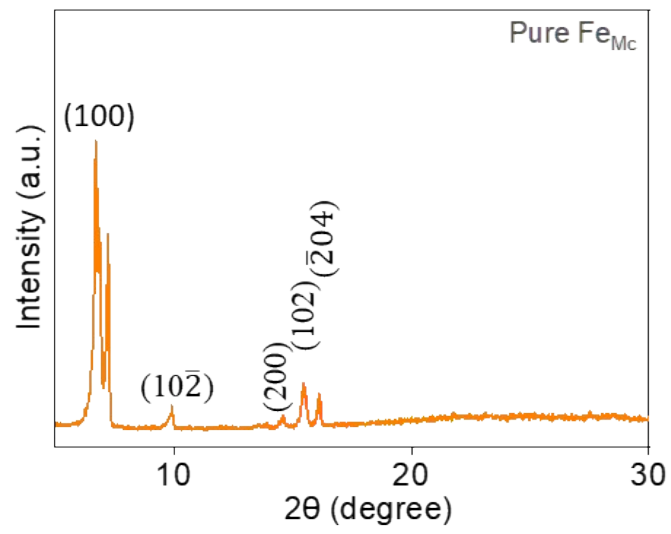
Figure S11. XRD pattern of Fe$_{Mc}$ material.
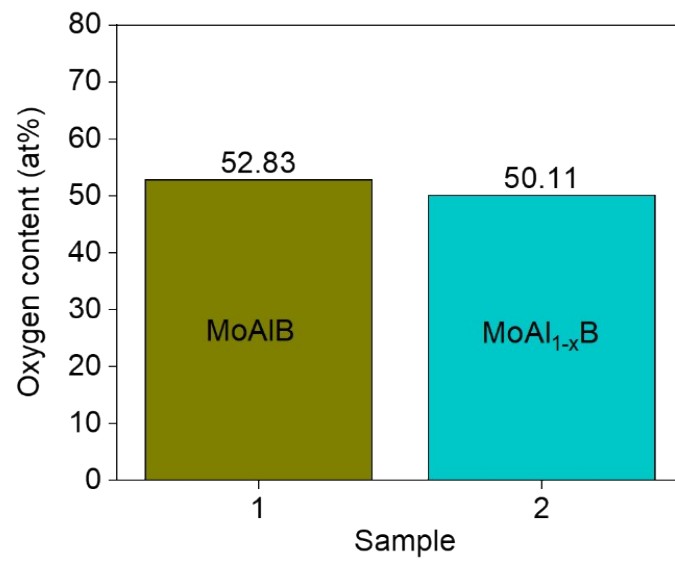
**Figure S12**. Surface oxygen content of MoAlB and MoAl$_{1-x}$B as identified by XPS analysis.
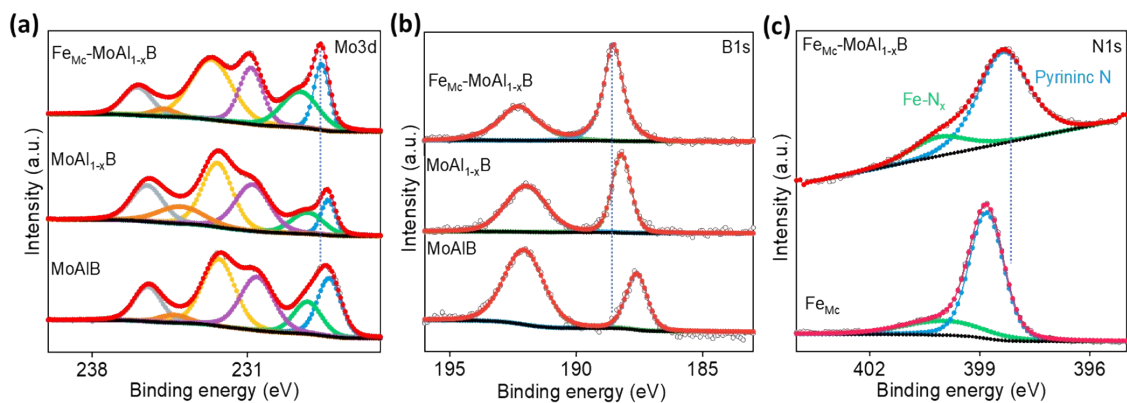
Figure S13. High resolution XPS spectra of (a) Mo3d, (b) B1s, and (c) N1s binding energies from MoAlB, MoAl$_{1-x}$B, and Fe$_{Mc}$–MoAl$_{1-x}$B materials.
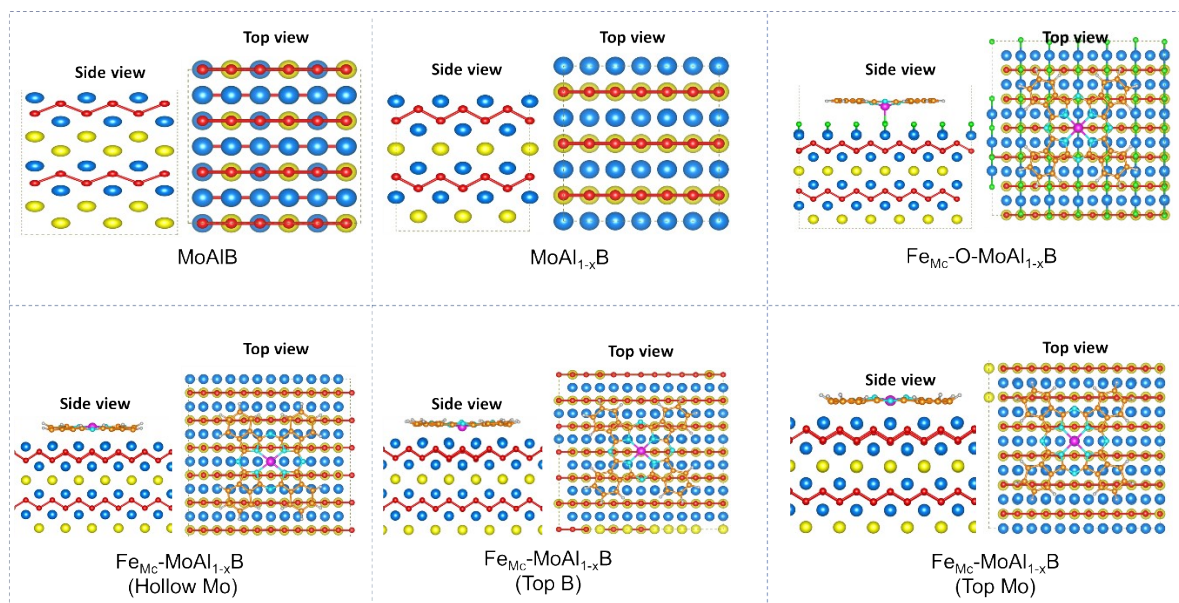
Figure S14. Side view and top view images for the MoAlB, MoAl$_{1-x}$B, adsorption of Fe$_{Mc}$ on MoAl$_{1-x}$B structure via Fe-O linking, an adsorption of Fe$_{Mc}$ on Hollow Mo, Top B, and Top Mo sites of the MoAl$_{1-x}$B structure.
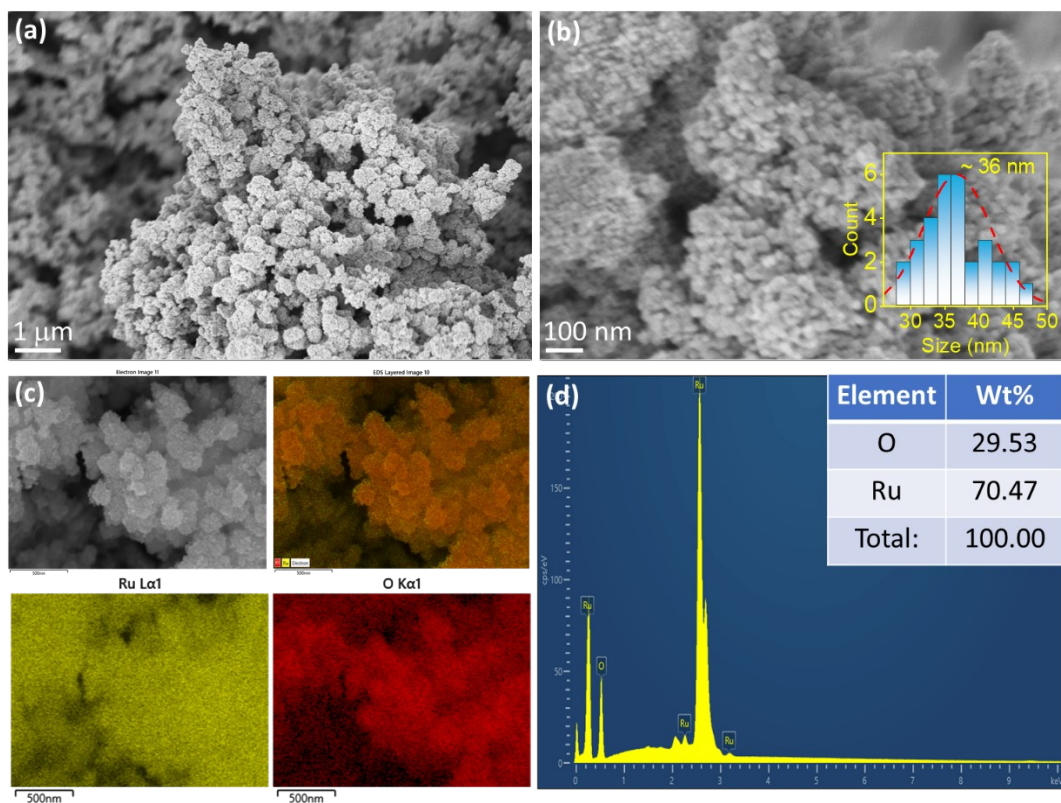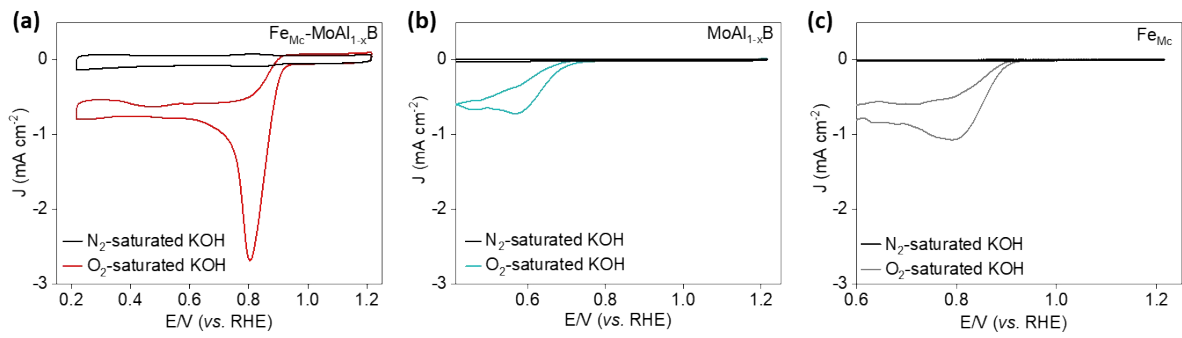
Figure S15. (a-b) SEM images (Inset: particle size distribution), (c) EDS mapping images, and (d) EDS spectrum of commercial RuO_2 catalyst.
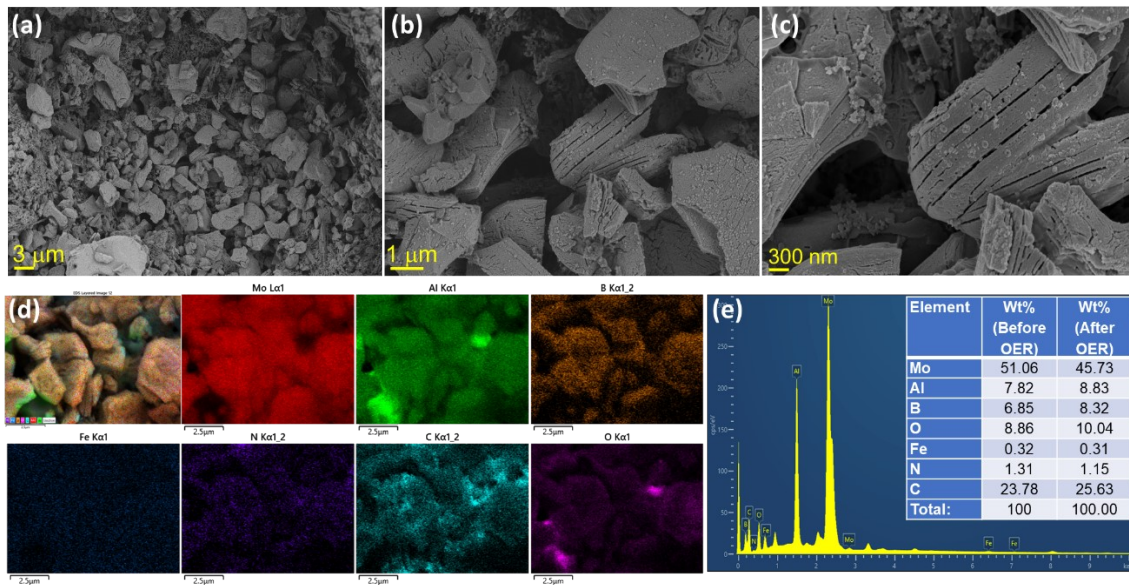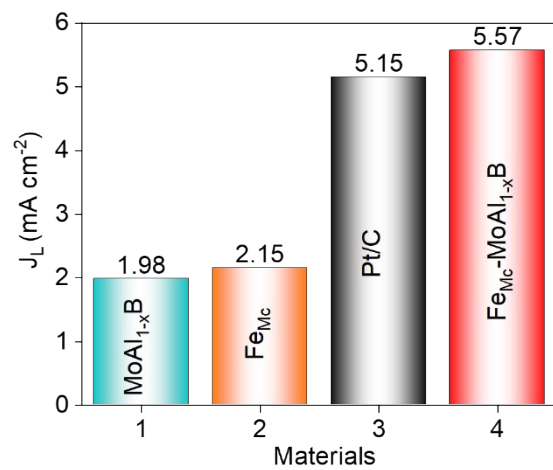
Figure S16. SEM and EDS results of the post-OER Fe_{Mc}–$MoAl_{1-x}B$-based electrode.
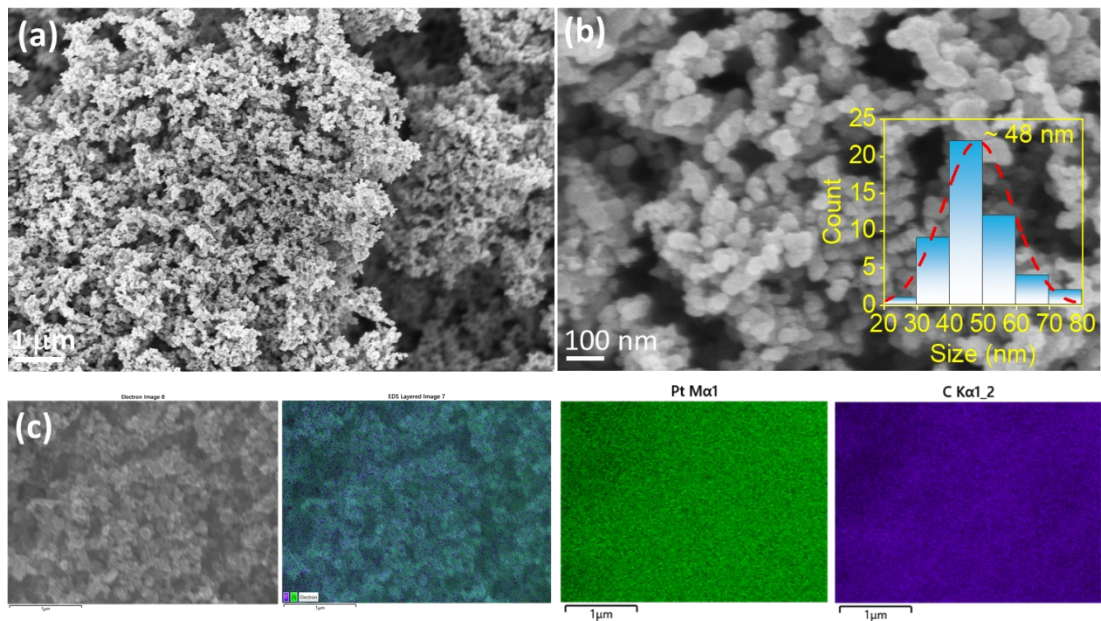
Figure S17. (a-b) SEM images (Inset: particle size distribution), (c) EDS mapping images of commercial Pt/C catalyst.
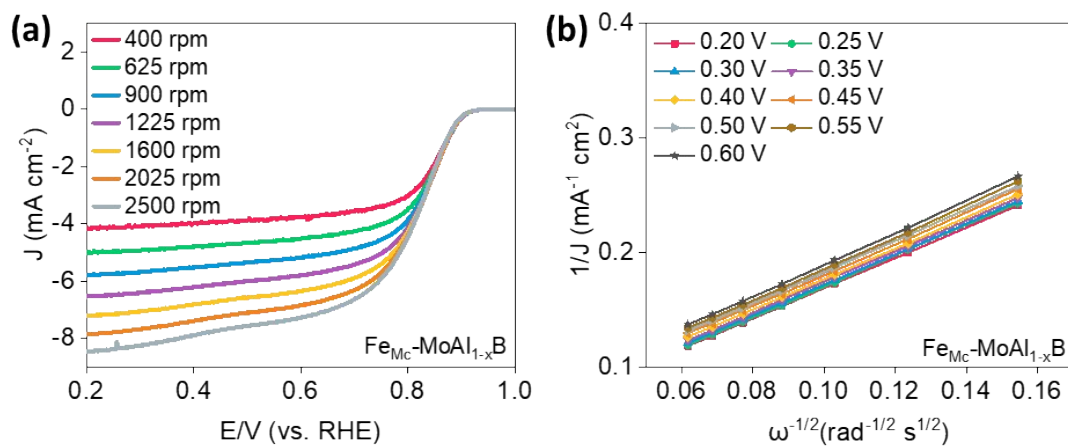
Figure S18. CV measurements of Fe_{Mc}–$MoAl_{1-x}B$, $MoAl_{1-x}B$, and Fe_{Mc} towards ORR at a scan rate of 50 mV s^{-1} in alkaline medium.
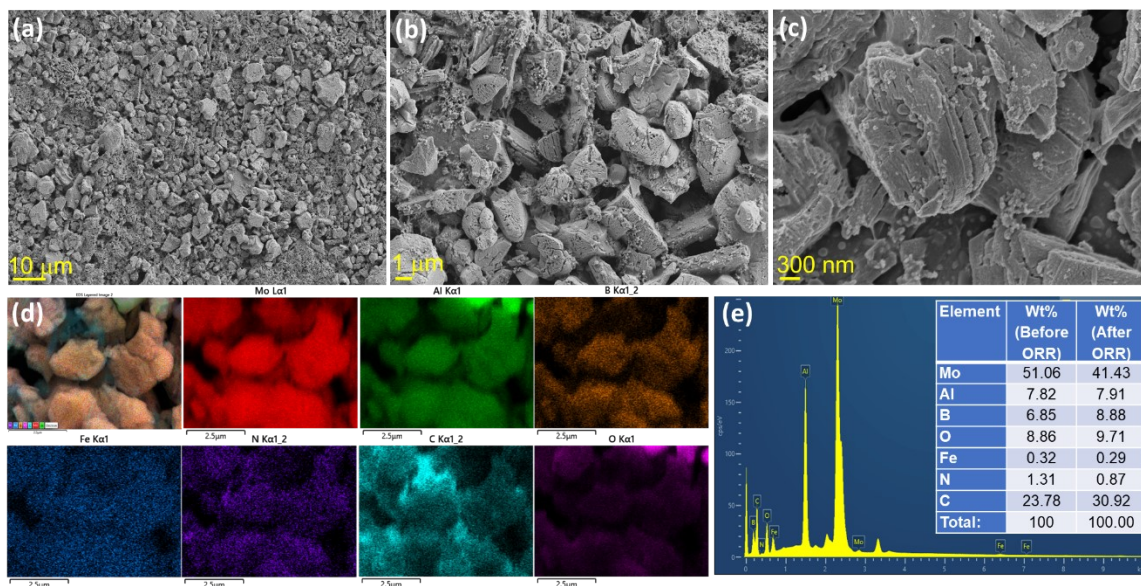
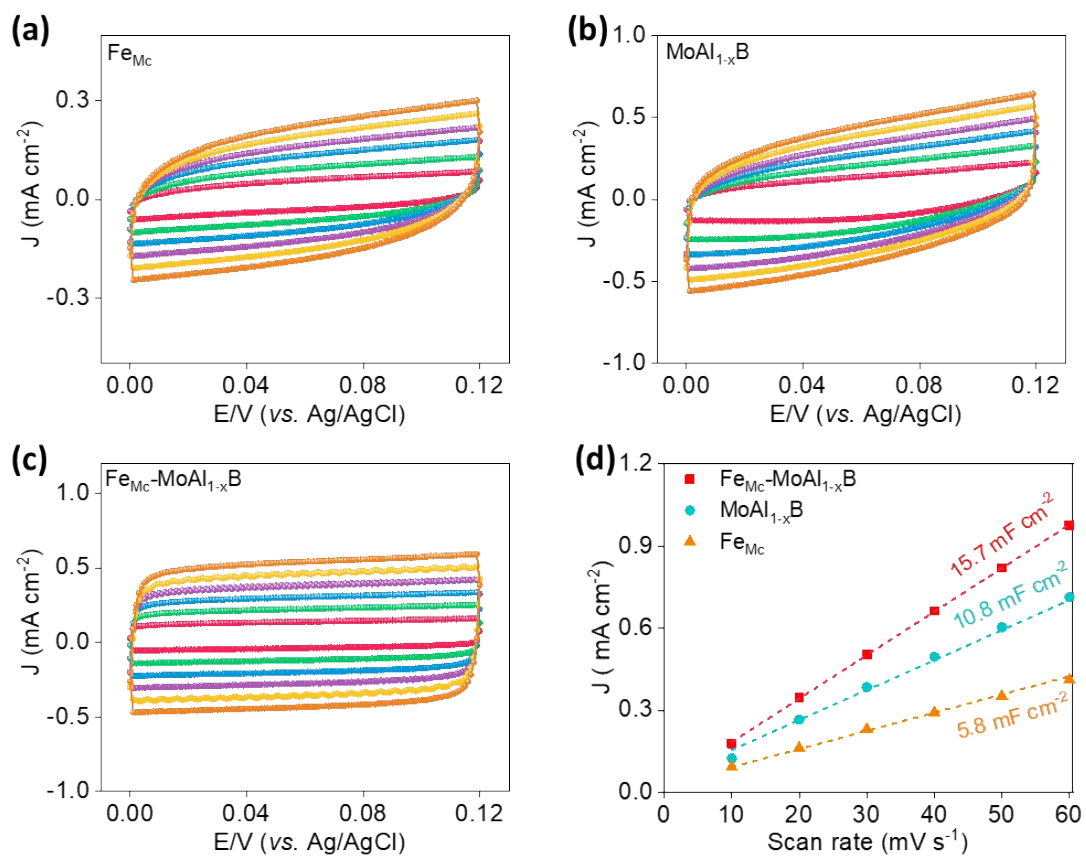**Figure S19**. Limit current density of different catalysts.

Figure S20. (a) LSV responses of Fe_{Mc}–$MoAl_{1-x}B$ at various rotation rates of the RDE electrode and (b) The linearity of Kautecky−Levich (K−L) plots at different potentials.

Figure S21. SEM and EDS results of the post-ORR Fe_{Mc}–$MoAl_{1-x}B$-based electrode.

**Figure S22**. CV responses of (a)) Fe_{Mc}, (b) $MoAl_{1-x}B$, and (c) $Fe_{Mc}–MoAl_{1-x}B$ at different scan rates in the non-faradaic potential range in alkaline medium; (d) C_{dl} values of) Fe_{Mc}, $MoAl_{1-x}B$, and $Fe_{Mc}–MoAl_{1-x}B$.
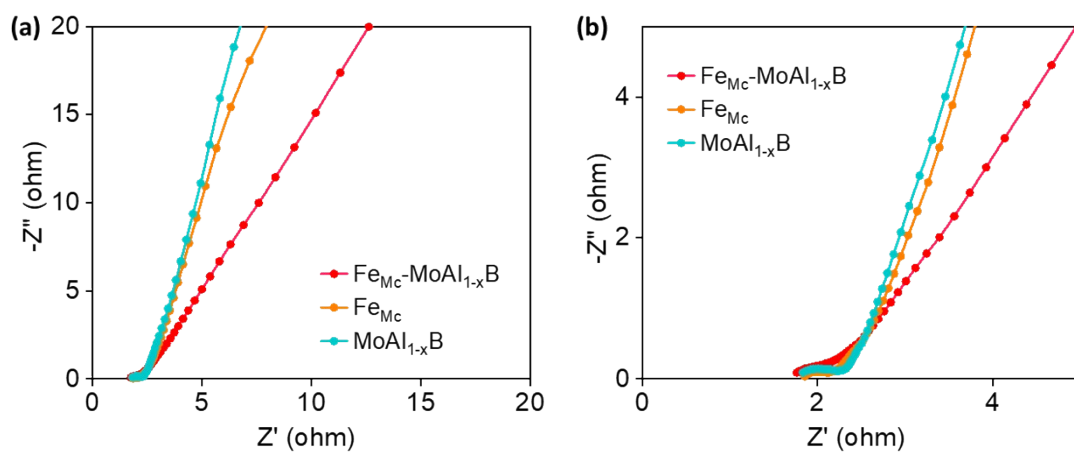
Figure S23. (a) EIS responses of Fe_{Mc}, $MoAl_{1-x}B$, and Fe_{Mc}–$MoAl_{1-x}B$ at open circuit potential (OCP) in alkaline medium.
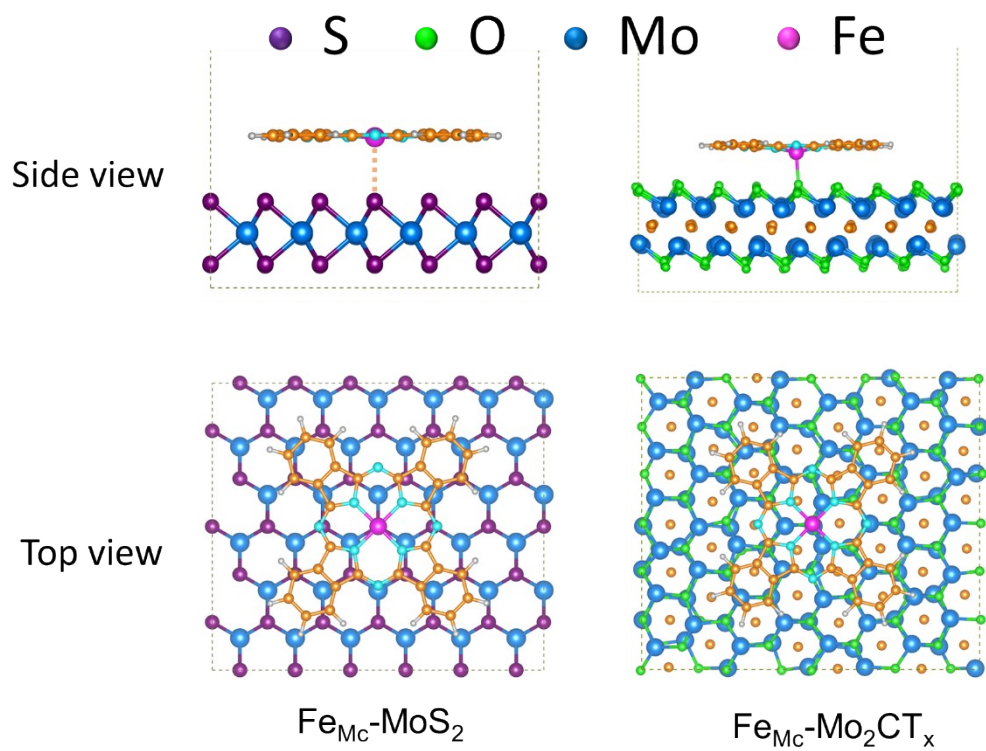
Figure S24. Structural model of hybrid derived from Fe_{Mc} assembling on MoS_2 and Mo_2CT_x MXene surfaces by DFT calculation.
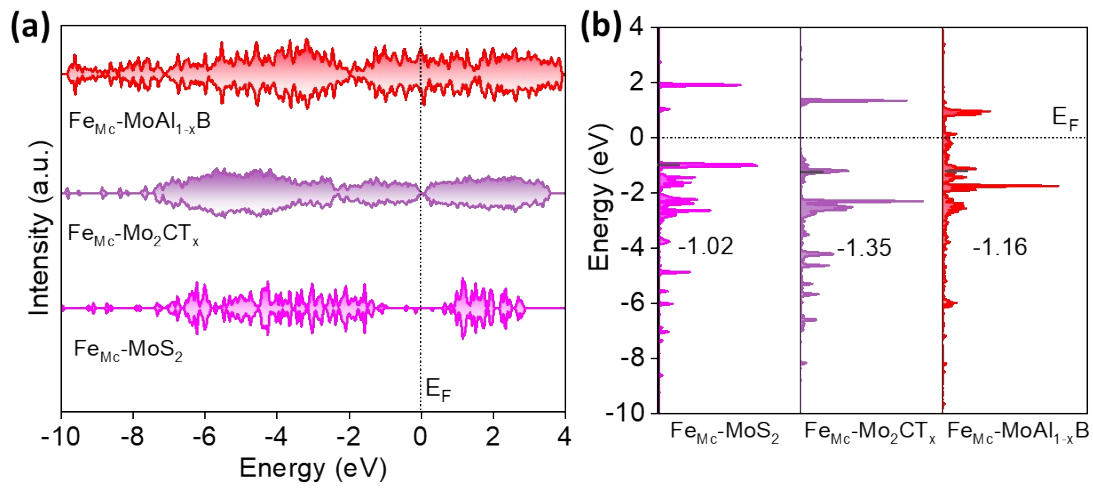
Figure S25. Comparison of (a) Total DOS and (b) Fe d-band center results from Fe_{Mc}–$MoAl_{1-x}B$, Fe_{Mc}–MoS_2, and Fe_{Mc}–Mo_2CT_x.
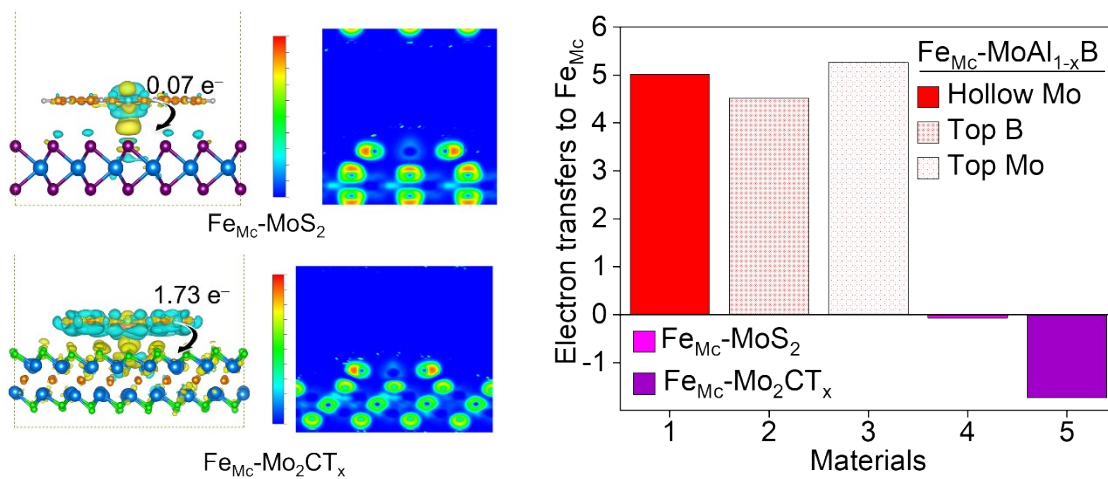
Figure S26. The charge transfer between the Fe_{Mc}–MoS_2 and Fe_{Mc}–Mo_2CT_x matrixes with Fe_{Mc}, as compared with that of the Fe_{Mc}–$MoAl_{1-x}B$.
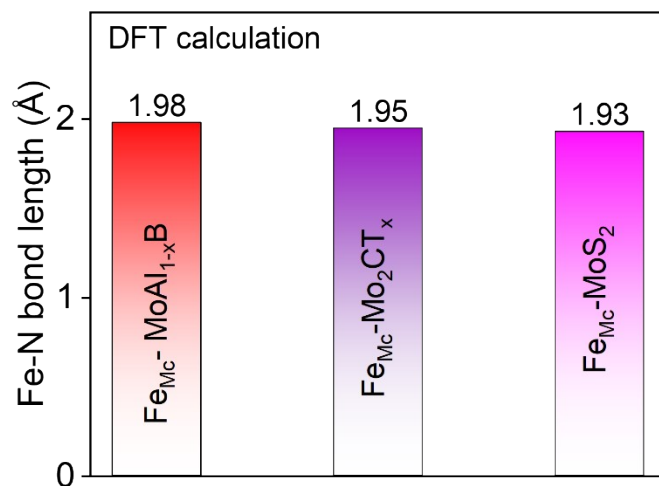
Figure S27. Comparison of of Fe–N bond length between Fe_{Mc}–$MoAl_{1-x}B$, Fe_{Mc}–MoS_2, and Fe_{Mc}–Mo_2CT_x by DFT calculation.
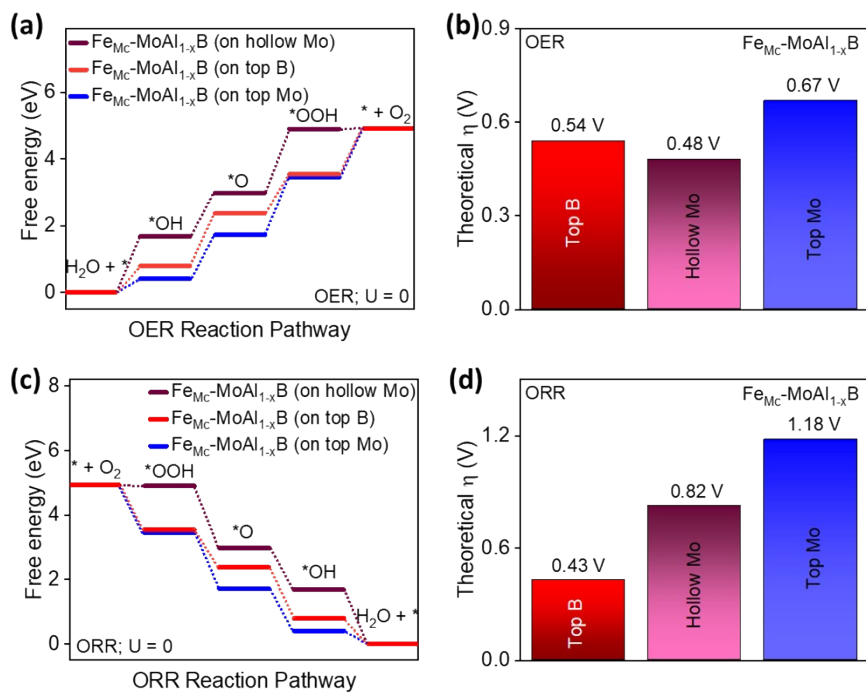
Figure S28. Free energy diagrams of Fe_{Mc}, $MoAl_{1-x}B$, and $Fe_{Mc}–MoAl_{1-x}B$ for (a) OER and (c) ORR; Theoretical η of Fe_{Mc}, $MoAl_{1-x}B$, and $Fe_{Mc}–MoAl_{1-x}B$ for (b) OER and (d) ORR.

33
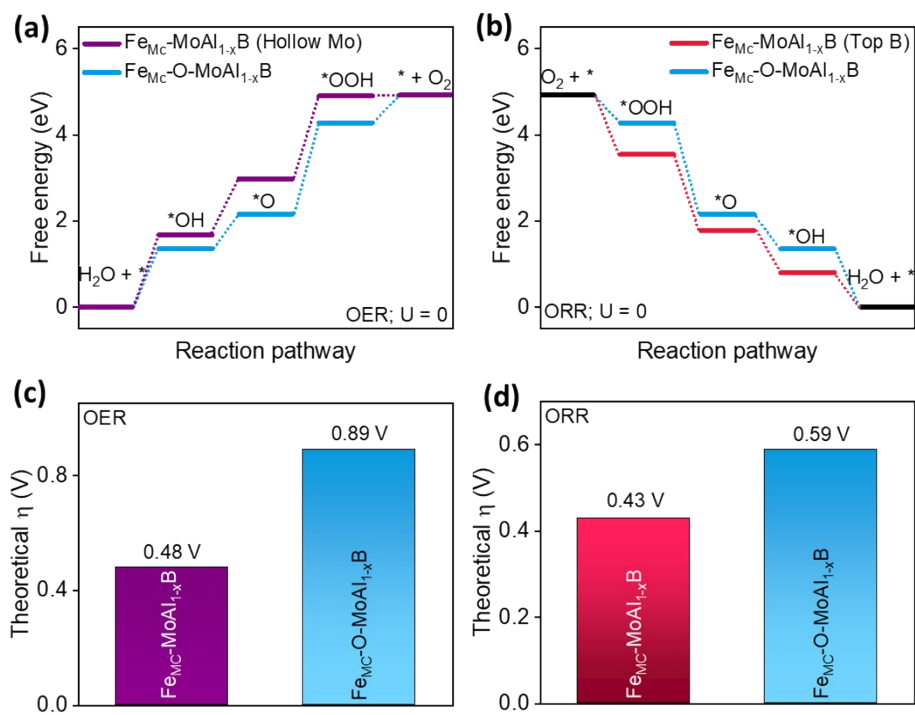
Figure S29. Free energy diagrams of $Fe_{Mc}–MoAl_{1-x}B$ and $Fe_{Mc}–O–MoAl_{1-x}B$ for (a) OER and (b) ORR; Theoretical η of $Fe_{Mc}–MoAl_{1-x}B$ and $Fe_{Mc}–O–MoAl_{1-x}B$ for (c) OER and (d) ORR.
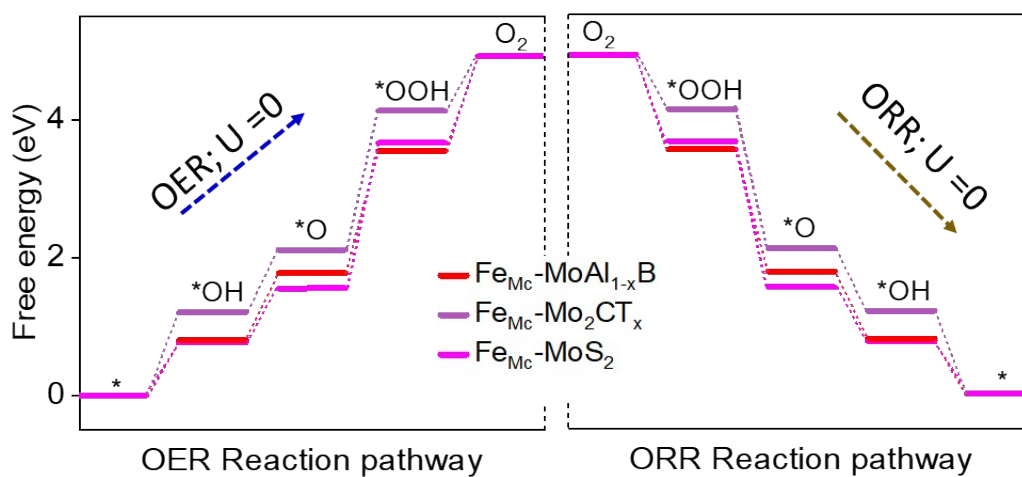
Figure S30. The ΔG behaviors of Fe_{Mc}–$MoAl_{1-x}B$, Fe_{Mc}–MoS_2, and Fe_{Mc}–Mo_2CT_x toward the OER and ORR.
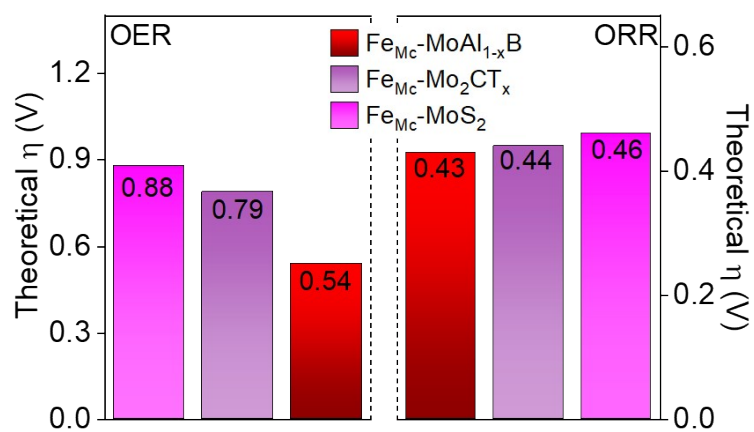
Figure S31. The theoretical overpotential of $Fe_{Mc}–MoAl_{1-x}B$, $Fe_{Mc}–MoS_2$, and $Fe_{Mc}–Mo_2CT_x$ toward the OER and ORR.
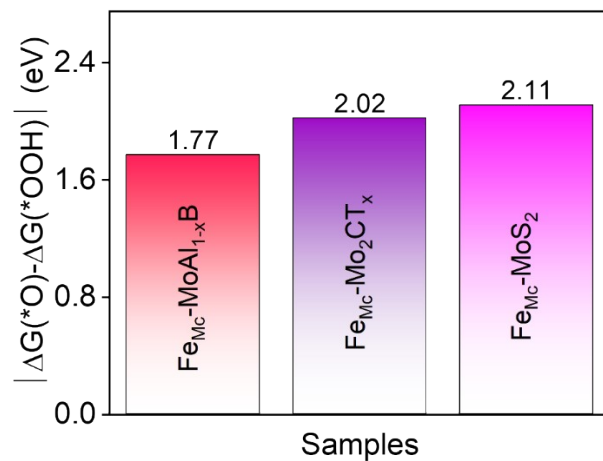
Figure S32. The $|\Delta G_{*O} - \Delta G_{*OOH}|$ difference of Fe_{Mc}–$MoAl_{1-x}B$, Fe_{Mc}–MoS_2, and Fe_{Mc}–Mo_2CT_x toward OER/ORR.
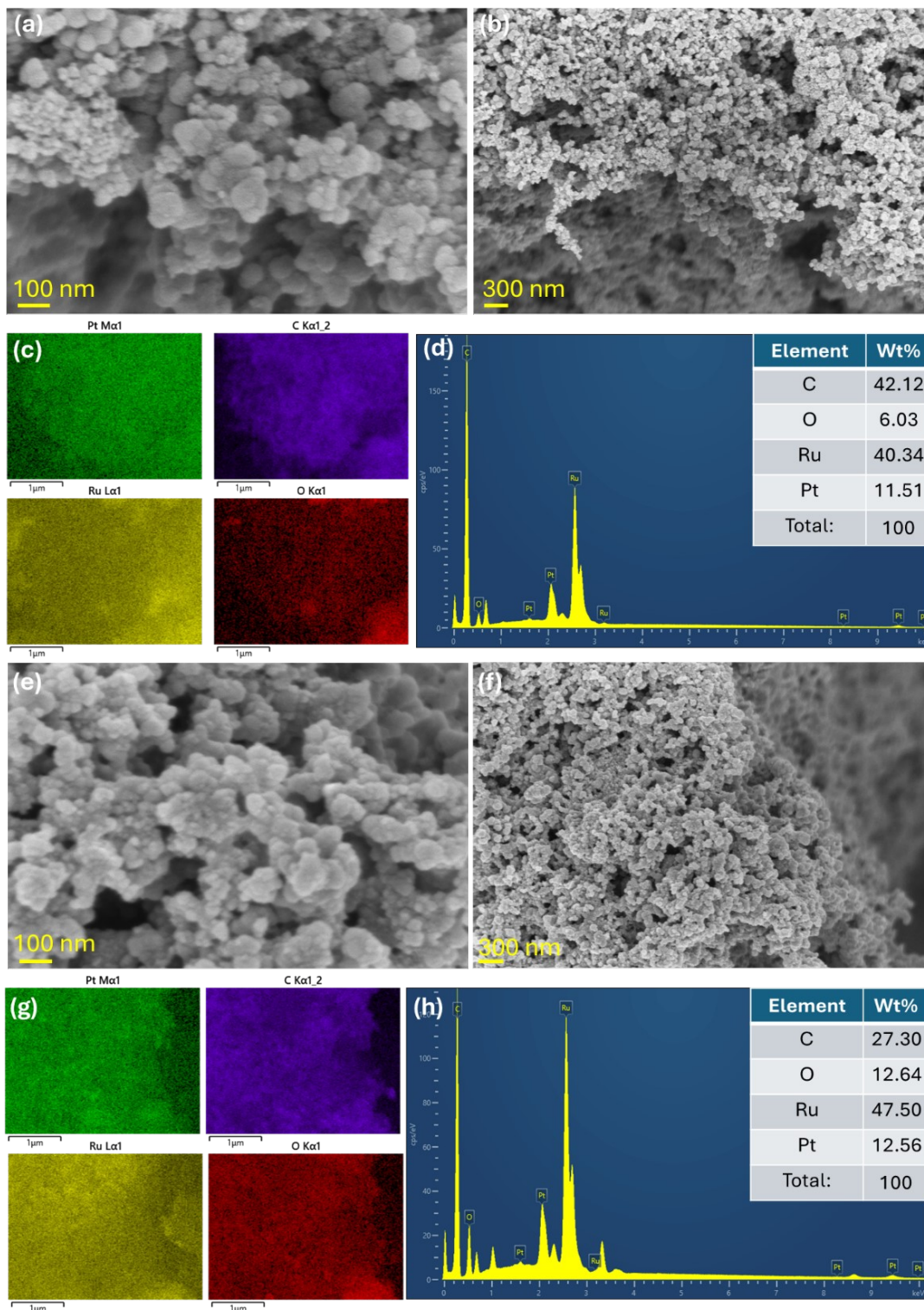
Figure S33. (a-b) SEM images, (c) EDS mapping, and (d) EDS spectrum of the pristine ($Pt/C+RuO_2$)-based electrode; (e-f) SEM images, (g) EDS mapping, and (h) EDS spectrum of the ($Pt/C+RuO_2$)-based electrode after cycling test.
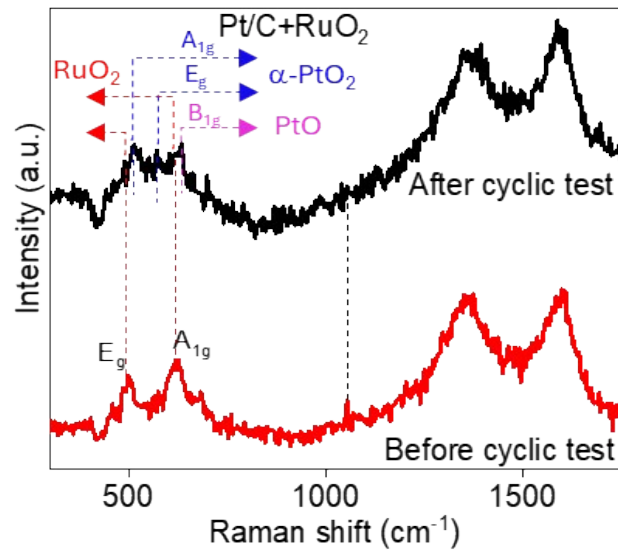
Figure S34. Raman analysis of the (Pt/C+RuO$_2$)-based electrode before and after cycling test.
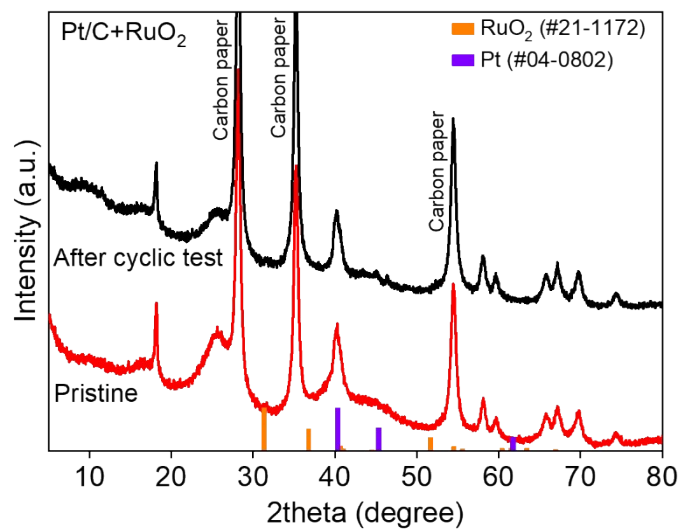
Figure S35. XRD analysis of the (Pt/C+RuO$_2$)-based electrode before and after cycling test.
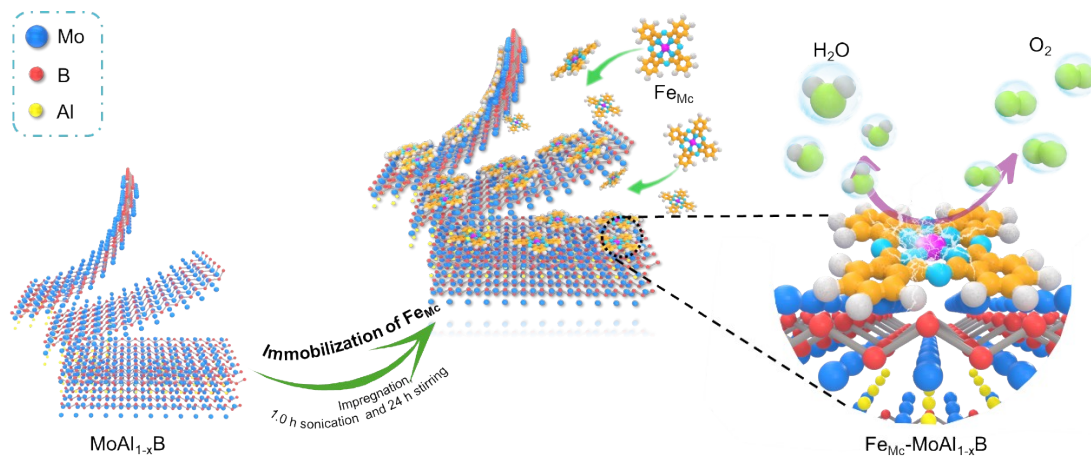
Figure S36. Illustration the fabrication of Fe_{Mc}–$MoAl_{1-x}B$ material based on Fe_{Mc} and delaminated $MoAl_{1-x}B$ for OER and ORR applications.

Table S1. Comparison of $\eta 10$ values between $Fe_{Mc}-MoAl_{1-x}B$ and recent reports towards OER in alkaline medium.

Materials	$\eta 10$ (mV)	References
$Fe_{Mc}-MoAl_{1-x}B$	356	This work
nm-CoO$_x$/N-RGO	370	Adv. Mater. 2019, 31, 1807468
CoO/hi-Mn$_3$O$_4$	378	Angew. Chem. 2017, 56, 8539-8543
CoS/CoO@NGNs	360	Nano-Micro Lett. 2021, 13, 3.
g-C$_3$N$_4$/CuZIF-67	410	Appl. Catal. B 2022, 306, 121096
CNTs-NC-CCC	380	Appl. Catal. B 2022, 319, 121937
C-MOF-C2-900	350	Adv. Mater. 2018, 30, 1705431
Fe/N-G-SAC	370	Adv. Mater. 2020, 32, 2003134
Ni-N$_4$/GHSs/Fe-N4	390	Adv. Mater. 2020, 32, 2004900
FCN$_4$-CNNT	420	Energy Storage Mater. 2023, 55, 397-405
SA-Fe-SNC@900	402	Adv. Mater. 2023, 35, 2209948
Fe,Co,N-C catalyst	410	*ACS Nano* 2022, 16, 5, 7890–7903
Fe-N$_x$-C	600	Adv. Funct. Mater. 2019, 29, 1808872
Fe-N$_4$ SAs/NPC	430	Adv. Mater. 2023, 35, 2303243
MoS$_2$@Fe-N-C	360	PNAS 2021, 118, e2110036118
FeNi/N-C-800	370	Appl. Catal. B 2023, 321, 122067
Co$_2$Fe$_1$@NC	420	J. Am. Chem. Soc. 2020, 142, 15, 7116-7127
CoFe-N-C	360	Nano Lett. 2022, 22, 8, 3392–3399
Fe−Se/NC	393	Angew. Chem. 2023, 62, e202219191

Table S2. Comparison of half-wave potential between $Fe_{Mc}-MoAl_{1-x}B$ and recent reports towards ORR in alkaline medium.

Materials	$E_{half-wave}$ (V)	References
$Fe_{Mc}-MoAl_{1-x}B$	0.862	This work
nm-CoO$_x$/N-RGO	0.896	Adv. Mater. 2019, 31, 1807468
CoS/CoO@NGNs	0.84	Nano-Micro Lett. 2021, 13, 3.
CNTs-NC-CCC	0.83	Appl. Catal. B 2022, 319, 121937
CoNi@NCNTs/CC	0.82	Appl. Catal. B 2022, 317, 121764
C-MOF-C2-900	0.82	Adv. Mater. 2018, 30, 1705431
NiCo$_{2.148}$O$_4$ PNSs	0.65	Adv. Mater. 2020, 32, 2001651
CoNC@LDH	0.84	Adv. Mater. 2021, 33, 2008606
Co-N,B-CSs	0.83	ACS Nano 2018, 12, 2, 1894–1901
Co/N-CNSNs	0.83	ACS Energy Lett. 2018, 3, 12, 2914–2920
Ni-N$_4$/GHSs/Fe-N$_4$	0.83	Adv. Mater. 2020, 32, 2003134
Fe/Ni-N$_x$/Cs	0.855	Adv. Mater. 2020, 22, 2004670
VC-MOF-Fe	0.753	Nano Energy 2021, 82, 105714
MoS$_2$@Fe-N-C	0.84	PNAS 2021, 118, e2110036118
FeNi/N-C-800	0.845 V	Appl. Catal. B 2023, 321, 122067
Co$_2$Fe$_1$@NC	0.85	J. Am. Chem. Soc. 2020, 142, 15, 7116-7127
CoFe–N–C	0.86	ACS Nano 2022, 16, 8, 11944–11956

Table S3. Comparison of ZAB performance between Fe_{Mc}–$MoAl_{1-x}B$ air cathode and recent reports.

Materials	OCV (V)	P (mW cm^{-2})	Capacity (mAh·g^{-1}$_{Zn}$)	Stability	References
Fe_{Mc}–$MoAl_{1-x}B$	1.55	168.2	734.4@10 mA cm^{-2}	800 h	This work
N-GCNT/FeCo	1.48	89	872.2@100 mA cm^{-2}	40 h	Adv. Energy Mater. 2017, 7, 1602420
$Fe-N_x-C$	1.51	96.4	734.4@10 mA cm^{-2}	300 h with an initial round-trip efficiency of 59.6%	Adv. Funct. Mater. 2019, 29, 1808872
FeNC–S–Fe_xC/Fe	1.41	149.4	663@10 mA cm^{-2}	over 380 cycles (48 h) at 2.0 mA cm^{-2}	Adv. Mater. 2018, 30, 1804504
Co/Co_3O_4@PGS	1.45	118.3	---	800 h	Adv. Energy Mater., 2018, 8, 1702900
CoS/CoO@NGNs	1.45	137.8	723.9@20 mA cm^{-2}	100 h	Nano-Micro Lett., 2020, 13, 1-15
Fe SA/NCZ	1.441	101	---	for >44 h cycling test at 2 mA cm^{-2}	Adv. Funct. Mater. 2023, 33, 2213897
CoNi@NCNTs/CC	1.49	138	782@10 mA cm^{-2}	370 h	Appl. Catal. B 2022, 317, 121764
$Co-N_x-C$	1.439	152	749.4@20 mA	---	Adv. Mater. 2017, 29, 1703185

			cm^{-2}		
C-MOF-C2-900	1.46	105	741@10 mA cm^{-2}	40 h at 5 and 10 mA cm^{-2}	Adv. Mater. 2018, 30, 1705431
CoZn-NC-700	1.42	152	578@10 mA cm^{-2}	> 32 h (385 cycles)	Adv. Funct. Mater. 2017, 27, 1700795
NiCo$_{2.148}$O$_4$ PNSs	1.46	83	---	20 h	Adv. Mater. 2020, 32, 2001651
CoSAs-NGST	1.49	148	---	133 h (399 cycles) @5 mA cm^{-2}	Adv. Funct. Mater. 2021, 31, 2010472
Co-N,B-CSs	1.43	100.4	---	128 cycles for 14 h of operation	ACS Nano 2018, 12, 2, 1894–1901
Co/N-CNSNs	1.471	81.7	638.4@10 mA cm^{-2}	100 continuous cycles (over 33 h) for	ACS Energy Lett. 2018, 3, 12, 2914–2920
CoFe–N–C	1.49	142.1	---	200 h@5 mA cm^{-2}	Nano Lett. 2022, 22, 8, 3392–3399
MS-CoSA-N-C	1.43	160	760@10 mA cm^{-2}	250 cycles@10 mA cm^{-2}	ACS Nano 2022, 16, 8, 11944–11956
3D SAFe	1.47	156	815@10 mA cm^{-2}	80 h (57 mV decrease)	Nano Lett. 2022, 22, 18, 7386–7393
Fe/Ni-Nx/Cs	1.525	148	712@50 mA cm^{-2}	312 h, 300 cycles at 20 mA cm^{-2}	Adv. Mater. 2020, 32, 2004670
VC-MOF-Fe	1.49	113	---	26 h	Nano Energy 2021, 82, 105714

CCNF-PDIL SSEs	1.46	135	700@5 mA cm^{-2}	240 h for 720 cycles	Angew. Chem. 2022, 61, e202117703
Fe$_x$/Cu–N@CF	1.4	156	1110.4@100 mA cm^{-2}	100 h with only 70 mV of voltage decay	Energy Environ. Sci., 2023, 16, 3576-3586
MoS$_2$@Fe-N-C	1.47	78	442@5 mA cm^{-2}	50 cycles@5 mA·cm^{-2}	PNAS 118 (40), 2021, e2110036118
FeNi/N-C-800	1.46	115	806@5 mA cm^{-2}	500 cycles/1000 h	Appl. Catal. B 2023, 321, 122067
Fe0.5Co0.5Ox	1.44	86	709@25 mA cm^{-2}	Over 120 h@10 mA·cm^{-2}	Adv. Mater. 2017, 29, 1701410
Fe−Se/NC	1.47	135	764@@5 mA cm^{-2}	200 h (1090 cycles)	Angew. Chem. 2023, 62, 15, e202219191

References

[1]   S. J. Park, T. H. Nguyen, D. T. Tran, V. A. Dinh, J. H. Lee, N. H. Kim, *Energy Environ Sci* **2023**, *16*, 4093.

[2]   J. Halim, S. Kota, M. R. Lukatskaya, M. Naguib, M. Q. Zhao, E. J. Moon, J. Pitock, J. Nanda, S. J. May, Y. Gogotsi, M. W. Barsoum, *Adv Funct Mater* **2016**, *26*, 3118.

[3]   T. H. Nguyen, P. K. L. Tran, V. A. Dinh, D. T. Tran, N. H. Kim, J. H. Lee, *Adv Funct Mater* **2023**, *33*, 2210101.

[4]   G. Kresse, J. Furthmiiller, *Comput Mater Sci* **1996**, *6,* 15-50.

[5]   G. Kresse, J. Furthmü, *Phys Rev B* **1996,** *54,* 11169.

[6]   J. P. Perdew, K. Burke, M. Ernzerhof, *Phys Rev Lett.* **1996***, 77,* 3865.

[7]   S. Grimme, J. Antony, S. Ehrlich, H. Krieg, *J Chem Phys* **2010**, *132*, 154104.

[8]   V. Wang, N. Xu, J. C. Liu, G. Tang, W. T. Geng, *Comput Phys Commun* **2021**, *267*, 108033.

[9]   Q. Liang, G. Brocks, A. Bieberle-Hütter, *J Phys Energy* **2021**, *3*, 026001.

[10]   I. C. Man, H. Y. Su, F. Calle-Vallejo, H. A. Hansen, J. I. Martínez, N. G. Inoglu, J. Kitchin, T. F. Jaramillo, J. K. Nørskov, J. Rossmeisl, *ChemCatChem* **2011**, *3*, 1159.

[11]   D. Bury, M. Jakubczak, M. A. K. Purbayanto, M. Rybak, M. Birowska, A. Wójcik, D. Moszczyńska, K. Eisawi, K. Prenger, V. Presser, M. Naguib, A. M. Jastrzębska, *Adv Funct Mater* **2023**, *33*, 2308156.

[12]   Z. Li, Z. Zhuang, F. Lv, H. Zhu, L. Zhou, M. Luo, J. Zhu, Z. Lang, S. Feng, W. Chen, L. Mai, S. Guo, *Adv Mater* **2018**, *30*, 1803220.